

Atmospheric-Pressure Synthesis of 2D Nitrogen-Rich Tungsten Nitride

Huimin Yu, Xin Yang, Xu Xiao, Ming Chen, Qinghua Zhang, Liang Huang, Jiabing Wu, Tianqi Li, Shuangming Chen, Li Song, Lin Gu, Bao Yu Xia, Guang Feng, Jia Li, and Jun Zhou*

2D transition metal nitrides, especially nitrogen-rich tungsten nitrides (W_xN_y , $y > x$), such as W_3N_4 and W_2N_3 , have a great potential for the hydrogen evolution reaction (HER) since the catalytic activity is largely enhanced by the abundant W–N bonding. However, the rational synthesis of 2D nitrogen-rich tungsten nitrides is challenging due to the large formation energy of W–N bonding. Herein, ultrathin 2D hexagonal- W_2N_3 (h - W_2N_3) flakes are synthesized at atmospheric pressure via a salt-templated method. The formation energy of h - W_2N_3 can be dramatically decreased owing to the strong interaction and domain matching epitaxy between KCl and h - W_2N_3 . 2D h - W_2N_3 demonstrates an excellent catalytic activity for cathodic HER with an onset potential of -30.8 mV as well as an overpotential of -98.2 mV for 10 mA cm^{-2} .

As an emerging family of 2D materials, 2D transition metal nitrides (TMNs), such as V_2N , MoN , W_2N , and GaN etc., have been widely sought in the fields of energy storage, catalysis, and optoelectronics due to their excellent physical and chemical properties.^[1–7] Notably, 2D nitrogen-rich TMNs as an infrequent group are of particular interest owing to the distinctive properties turned out by the increasing ratio of nitrogen to metal.^[8] In general, nitrogen-rich tungsten nitrides such as W_2N_3 and W_3N_4 are decent candidates for hydrogen evolution reaction (HER) because the electrical structure of W atoms can be tuned by nitrogen atoms, with the catalytic activity largely

increasing by the abundant W–N bond. To the best of our knowledge, the experimental synthesis of 2D nitrogen-rich tungsten nitrides is not reported in literature because of the harsh synthesis condition, stemming from the sluggish reaction thermodynamics of penetrating nitrogen into tungsten lattice.^[9]

Overall, high pressure and temperature (P – T) synthetic method (5 GPa and 880–2570 K) was adopted to prepare various nitrogen-rich tungsten nitrides such as W_2N_3 , W_3N_4 .^[10] However, this harsh synthesis condition is laborious to control the morphology of tungsten nitrides, especially for the 2D structure.^[11–14] As an alter-

native strategy, ammoniating tungsten metals or compounds are extensively studied to produce tungsten nitrides.^[9,15] Yet, the reaction is always incomplete, leading to low nitrogen ratio in final products with unreacted tungsten precursor (tungsten, tungsten oxides, etc.).^[16] Consequently, developing a facile and real-world synthetic strategy, with favorable reaction thermodynamics and facile morphology control for 2D nitrogen-rich tungsten nitrides, is highly desired but still thought provoking.

Herein, we synthesize atomically thin 2D nitrogen-rich hexagonal W_2N_3 (h - W_2N_3) nanosheets via salt-templated method at atmospheric pressure for the first time. In this strategy, h - W_2N_3

H. Yu, Dr. X. Xiao, Dr. L. Huang, J. Wu, Dr. T. Li, Prof. J. Zhou
Wuhan National Laboratory for Optoelectronics
Huazhong University of Science and Technology
Wuhan 430074, Hubei, P. R. China
E-mail: jun.zhou@mail.hust.edu.cn

X. Yang, Prof. J. Li
Laboratory for Computational Materials Engineering
Division of Energy and Environment
Graduate School at Shenzhen
Tsinghua University
Shenzhen 518055, Guangdong, P. R. China
M. Chen, Prof. G. Feng
State Key Laboratory of Coal Combustion
School of Energy and Power Engineering
Huazhong University of Science and Technology
Wuhan 430074, Hubei, P. R. China

Dr. Q. Zhang, Prof. L. Gu
Beijing National Laboratory for Condensed Matter Physics
and Institute of Physics
Chinese Academy of Sciences
Beijing 100190, P. R. China

Dr. S. Chen, Prof. L. Song
National Synchrotron Radiation Laboratory
CAS Center for Excellence in Nanoscience
University of Science and Technology of China
Hefei 230029, Anhui, P. R. China

Prof. B. Y. Xia
Key laboratory of Material Chemistry for Energy Conversion and Storage
(Ministry of Education)
Hubei Key Laboratory of Material Chemistry and Service Failure
School of Chemistry and Chemical Engineering
Huazhong University of Science and Technology
Wuhan 430074, Hubei, P. R. China

 The ORCID identification number(s) for the author(s) of this article can be found under <https://doi.org/10.1002/adma.201805655>.

DOI: 10.1002/adma.201805655

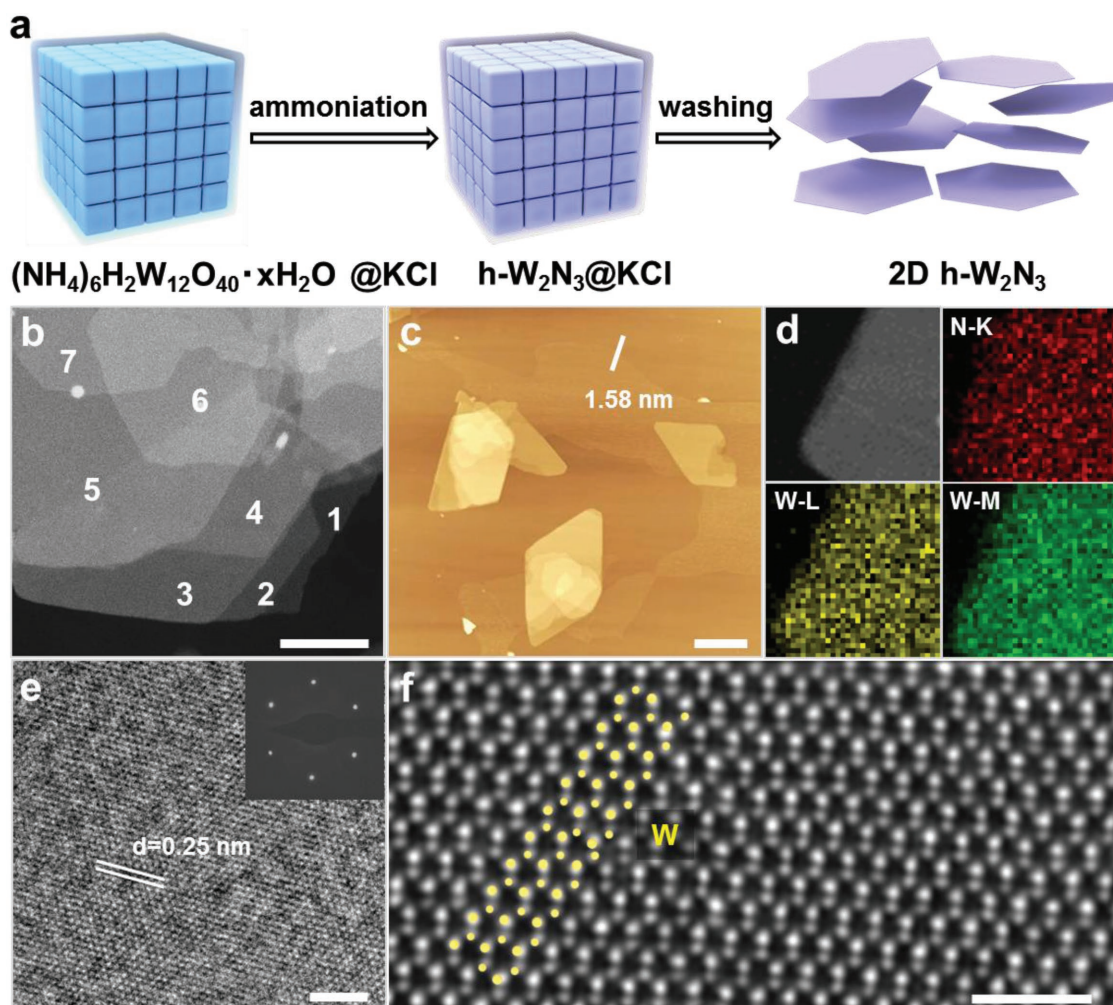


Figure 1. Synthesis process and characterization of 2D $h\text{-W}_2\text{N}_3$. a) Schematic representation of synthesis of 2D $h\text{-W}_2\text{N}_3$. $(\text{NH}_4)_6\text{H}_2\text{W}_{12}\text{O}_{40}\cdot x\text{H}_2\text{O}@KCl$ were slowly ammoniated in a NH_3 atmosphere to obtain 2D $h\text{-W}_2\text{N}_3$ flakes. b) STEM image of overlapping single-layer 2D $h\text{-W}_2\text{N}_3$ nanosheets. Scale bar: 200 nm. c) AFM image of the edge of 2D $h\text{-W}_2\text{N}_3$ nanosheets, thickness of ≈ 1.58 nm. Scale bar: 2 μm . d) EDS mapping of 2D $h\text{-W}_2\text{N}_3$ flake. e) HRTEM and SAED images of 2D $h\text{-W}_2\text{N}_3$. Lattice fringes with 0.25 nm interplanar spacing belong to the (100) facet. Scale bar: 2 nm. SAED confirmed the single hexagonal structure. f) HAADF-STEM of $h\text{-W}_2\text{N}_3$. Scale bar: 1 nm.

nanosheets can grow on the surface of KCl according to the domain matching epitaxy (DME),^[17] which is further elucidated by theoretical calculation. The interfacial formation energy of $h\text{-W}_2\text{N}_3$ on KCl can be reduced with introduction of the domain pattern, indicating the growth of $h\text{-W}_2\text{N}_3$ on KCl (002) facet is thermodynamically favorable. The 2D $h\text{-W}_2\text{N}_3$ flakes show superior catalytic activity for HER compared to its bulk counterpart.

Synthetic process for the 2D $h\text{-W}_2\text{N}_3$ nanosheets is illustrated in Figure 1a. First, $(\text{NH}_4)_6\text{H}_2\text{W}_{12}\text{O}_{40}\cdot x\text{H}_2\text{O}$ was uniformly coated on the surface of KCl ($(\text{NH}_4)_6\text{H}_2\text{W}_{12}\text{O}_{40}\cdot x\text{H}_2\text{O}@KCl$) to obtain the precursor. This precursor was ammoniated at 750 °C in a NH_3 atmosphere. Then KCl salt templates were dissolved and removed after rinsing in deionized water and filtration to obtain the 2D $h\text{-W}_2\text{N}_3$ flakes. The 2D morphology of $h\text{-W}_2\text{N}_3$ was identified by scanning electron microscopy (SEM) and aberration-corrected scanning transmission electron microscopy (STEM) (Figure S1, Supporting Information and Figure 1b). The lateral size of the flakes is of ≈ 5 μm . As can be seen in Figure 1b, seven layers of overlapped flakes still

showed high transparency, indicating the ultrathin feature of 2D $h\text{-W}_2\text{N}_3$. By measuring the edge of the flake, the thickness of 2D $h\text{-W}_2\text{N}_3$ is verified to be ≈ 1.5 nm, which is in accordance with the atomic force microscopy (AFM) measurement (≈ 1.58 nm, Figure S2, Supporting Information and Figure 1c). Besides, the energy-dispersive spectroscopy (EDS) mapping of 2D $h\text{-W}_2\text{N}_3$ nanosheets shown in Figure 1d reveals the uniform distribution of W and N. High-resolution transmission electron microscopy (HRTEM) and selected area electron diffraction (SAED) studies are carried out to verify the orientation and crystal quality of 2D $h\text{-W}_2\text{N}_3$ (Figure 1e). Single-crystalline hexagonal structure was confirmed with an interplanar spacing of 0.25 nm that belongs to the (100) facet. The high-angle annular dark-field scanning transmission electron microscopy (HAADF-STEM) was used to elucidate the atomic arrangement of $h\text{-W}_2\text{N}_3$ flakes (Figure 1f), external and internal layers of tungsten atoms can be clearly identified and well organized to the hexagonal lattice, consistent with the structure of $h\text{-W}_2\text{N}_3$ (inset, Figure 1f, Figure S3, Supporting Information). X-ray

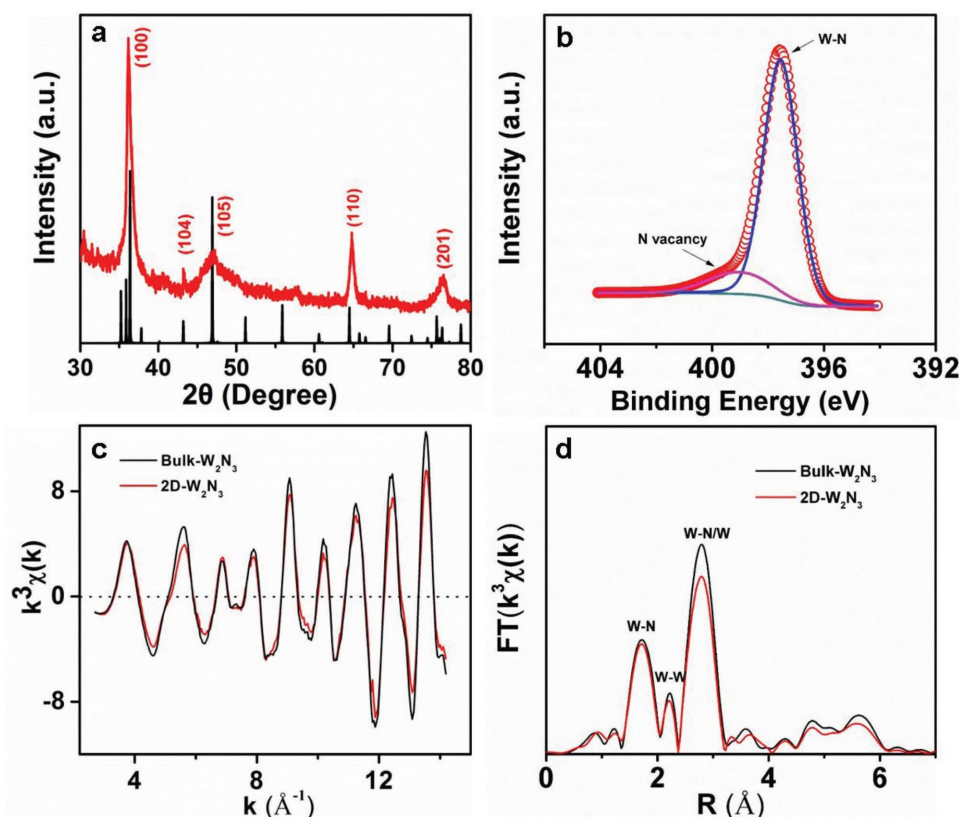


Figure 2. Crystal and surface characterization of 2D h - W_2N_3 . a) XRD pattern of 2D h - W_2N_3 powder. b) N 1s XPS spectrum of 2D h - W_2N_3 . c) W L_3 -edge extended XAFS oscillation function $k^3\chi(k)$. d) The corresponding Fourier transforms $FT(k^3\chi(k))$. The coordination numbers of W–W and W–N decreased remarkably, demonstrating unsaturated coordination of W atoms.

diffraction (XRD) pattern further confirmed the crystal structure of h - W_2N_3 ,^[10] where the main peak of (100) is in accordance with the HRTEM characterization in Figure 2a.

The X-ray photoelectron spectroscopy (XPS) was employed to probe the elemental composition of h - W_2N_3 . The W 4f spectra exhibits peaks at ≈ 35.1 and ≈ 33.0 eV, corresponding to the W $4f_{5/2}$ and W $4f_{7/2}$ characteristic peaks of 2D h - W_2N_3 , respectively. Another W peak appearing at ≈ 37.8 eV was due to a low surface oxidation in the storage period before XPS analysis, similar to the case of WS_2 (Figure S4, Supporting Information).^[18,19] The N 1s spectrum exhibited a peak at ≈ 397.5 eV which can be assigned to W–N bonding. Moreover, we found another peak at ≈ 399.0 eV which could be contributed to nitrogen atoms near the nitrogen vacancies (Figure 2b).^[20] To shed light on the local atomic arrangement and specific bonding modes of 2D h - W_2N_3 nanosheets, synchrotron radiation X-ray absorption fine structure (XAFS) measurements at the W L_3 -edge were performed. The W L_3 -edge extended XAFS (EXAFS) spectra for 2D and bulk h - W_2N_3 (the XRD and SEM were shown in Figure S5 in the Supporting Information) exhibited almost the same charge states, demonstrating the same crystal structure of both samples (Figure S6, Supporting Information). As shown in Figure 2c, the W L_3 -edge oscillation curve of h - W_2N_3 nanosheets demonstrated a difference in the peak intensity compared to the bulk counterpart, which is attributed to the decreased W–N and W–W coordination due to the reduced thickness of 2D h - W_2N_3 .^[21] This is also confirmed by the corresponding Fourier transform (FT)

$k^3\chi(k)$ functions (Figure 2d), qualitatively indicating their distinct local atomic arrangement. The least-squares curve fitting was conducted to acquire quantitative structural parameters around W atoms (Figure S7, Supporting Information) and the corresponding fitting results are shown in Table 1. The coordination numbers for W–W and W–N decreased (the W–N coordination numbers decrease from 3.0 and 2.8 to 2.7 and 2.3, respectively), while their disorder degrees increased compare with bulk counterpart, demonstrating partial dangling bonds and distortion on their surface. In another words, there are some vacancies in 2D h - W_2N_3 . This result fairly agrees with the XPS analysis that vacancies probably come from N. The generation of N vacancies on the surface of 2D h - W_2N_3 is attributed to the increased

Table 1. EXAFS curve-fitting results.

Sample	Path	N	R [Å]	σ^2 [10^{-3} Å ²]
Bulk W_2N_3	W–N	3.0	2.10	1.9
	W–W	0.9	2.62	3.8
	W–W	4.1	2.89	2.9
	W–N	2.7	3.60	4.7
2D W_2N_3	W–N	2.8	2.10	2.0
	W–W	0.7	2.61	4.7
	W–W	3.3	2.90	3.1
	W–N	2.3	3.62	4.4

surface energy of 2D morphology, which has been observed in additional 2D metal nitrides.^[22]

The XRD pattern of KCl was shown in Figure S8a in the Supporting Information, which is a cubic crystal, $a = 6.2917 \text{ \AA}$ (PDF: 00-041-1476). The SEM image (Figure S8b, Supporting Information) presents the cubic morphology and the lateral size is over 100 \mu m . The (002) facet of KCl is exposed to be the substrate for the growth of $h\text{-W}_2\text{N}_3$. However, the primitive lattice of $h\text{-W}_2\text{N}_3$ (001) surface with threefold rotational symmetry could not match with that of KCl substrate with fourfold rotational symmetry owing to the large lattice mismatch ($a(\text{KCl}) = 6.2917 \text{ \AA}$, $a(\text{W}_2\text{N}_3) = 2.90 \text{ \AA}$) and different rotational symmetry. Generally, for epitaxial growth in large-lattice mismatch systems, domains comprised of several lattice constants of epilayer match with those of the substrate, which is assigned to DME. In this case, the formation energy of the interface can be reduced. To determine the structure of $h\text{-W}_2\text{N}_3$ on KCl substrate, we built five possible interfacial structures with different W/K ratios (Figure 3a) for the purpose of reducing the lattice mismatch between $h\text{-W}_2\text{N}_3$ (001) and KCl(002) substrate as small as possible. The formation energies of the interfacial structures, denoted as $E_{\text{form}}(\text{interface})$, are calculated with respect to the total energies of clean KCl(002) surface ($E_{\text{tot}}(\text{KCl})$) and the primitive cell of monolayer 2D $h\text{-W}_2\text{N}_3$ ($E_{\text{tot}}(\text{W}_2\text{N}_3)$), normalized per formula unit of $h\text{-W}_2\text{N}_3$

$$E_{\text{form}}(\text{interface}) = [E_{\text{tot}}(\text{interface}) - E_{\text{tot}}(\text{KCl}) - nE_{\text{tot}}(\text{W}_2\text{N}_3)] / n \quad (1)$$

It is shown in Figure 3d and Table S1 in the Supporting Information that, except for pattern (5) with $E_{\text{form}}(\text{interface})$

of $0.13 \text{ eV}/h\text{-W}_2\text{N}_3$, all other interfacial structures have negative $E_{\text{form}}(\text{interface})$, which indicates the epitaxial growth of these patterns is energetically favorable. To further understand the origin of the stabilization of $h\text{-W}_2\text{N}_3$ by introducing KCl substrates, we employed Born–Haber analysis^[23] to decompose the $E_{\text{form}}(\text{interface})$ into two terms, the adhesive energy of monolayer $h\text{-W}_2\text{N}_3$ ($E_{\text{adh}} = [E_{\text{tot}}(\text{interface}) - E_{\text{tot}}(\text{KCl}) - E_{\text{free}}(\text{W}_2\text{N}_3)]/n$) and the formation energy of strained free-standing monolayer $h\text{-W}_2\text{N}_3$ ($E_{\text{form}}(\text{W}_2\text{N}_3) = [E_{\text{free}}(\text{W}_2\text{N}_3) - nE_{\text{tot}}(\text{W}_2\text{N}_3)]/n$). The adhesive energy term E_{adh} describes the interaction of monolayer $h\text{-W}_2\text{N}_3$ and KCl substrate, which can stabilize the interfaces. As shown in Figure 3b, E_{adh} correlates linearly with the average height of monolayer $h\text{-W}_2\text{N}_3$ above the substrates, which reveals monolayer $h\text{-W}_2\text{N}_3$ in the five structures can be easily adhesive to the KCl surface. While $E_{\text{form}}(\text{W}_2\text{N}_3)$ reflects the deformation degree of monolayer $h\text{-W}_2\text{N}_3$ in comparison with its counterpart without substrate, destabilizing the interfacial structures. There is a quadratic function relationship between $E_{\text{form}}(\text{W}_2\text{N}_3)$ and S/S_0 , where S and S_0 denote the area of strained free-standing and pristine monolayer $h\text{-W}_2\text{N}_3$, respectively. In spite of a large $E_{\text{form}}(\text{W}_2\text{N}_3)$ of pattern (5), the other four structures have much lower $E_{\text{form}}(\text{W}_2\text{N}_3)$, which indicates a low distortion of $h\text{-W}_2\text{N}_3$ on KCl (Figure 3c). On the whole, among all the interfacial structures, pattern (3) has the most negative $E_{\text{form}}(\text{interface})$ of $-0.22 \text{ eV}/h\text{-W}_2\text{N}_3$, owing to the next-smallest distance between the film and substrate and least deformation degree of $h\text{-W}_2\text{N}_3$. In conclusion, the strong interaction between $h\text{-W}_2\text{N}_3$ and KCl offers the driving force and a domain of monolayer $h\text{-W}_2\text{N}_3$ with small strain guarantees low resisting force for the atmospheric-pressure synthesis of 2D $h\text{-W}_2\text{N}_3$.

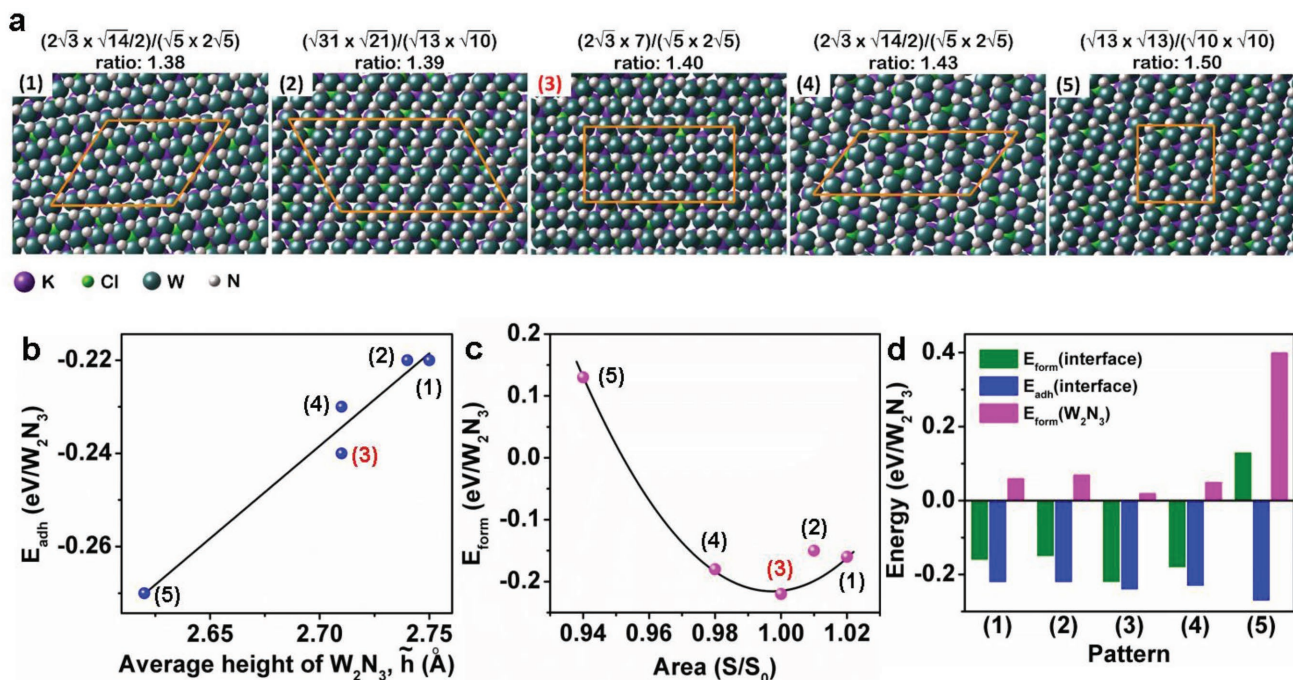


Figure 3. Geometrical structures and energetics of different interfacial structures. a) Five interfacial structures of monolayer $h\text{-W}_2\text{N}_3$ on KCl (002) substrate. The ratio of W/K is given for each structure. The orange box denotes the boundaries of the unit cells. The purple, bright green, dark green, and white balls represent potassium, chlorine, tungsten, and nitrogen atoms, respectively. b) The adhesive energy of monolayer $h\text{-W}_2\text{N}_3$ (E_{adh}) as the function of the average height of monolayer $h\text{-W}_2\text{N}_3$ above the KCl substrates (\bar{h}). c) The formation energy of strained free-standing monolayer $h\text{-W}_2\text{N}_3$ ($E_{\text{form}}(\text{W}_2\text{N}_3)$) as the function of the ratio of lateral area of $h\text{-W}_2\text{N}_3$ compared to that of pristine $h\text{-W}_2\text{N}_3$. d) Energies of five interfacial structures.

To profoundly verify the mechanism in the synthesizing process, several experiments were performed. Direct ammoniating $(\text{NH}_4)_6\text{H}_2\text{W}_{12}\text{O}_{40} \cdot x\text{H}_2\text{O}$ powder under same condition without KCl template could obtain WO_3 with few tungsten nitrides at atmospheric pressure (Figure S9, Supporting Information). In addition, it was confirmed the importance of DME in our method by using other salts as templates (e.g., NaCl). As expected, after changing the template by NaCl, the final product shows thick plate morphology, and still mainly remained WO_3 phase with few tungsten nitrides (Figure S10a,b, Supporting Information). Accordingly, it was that the interfacial structures with DME between KCl and 2D $h\text{-W}_2\text{N}_3$ can dramatically drop the formation energy, leading to a favorable 2D growth condition with confinement effect. It is a key factor for the formation of ultrathin 2D $h\text{-W}_2\text{N}_3$.

Atomically thin nanosheets with dramatic conductivity and abundant active sites are considered as the promising catalysts for HER. Herein, the HER activity of 2D $h\text{-W}_2\text{N}_3$ flakes was investigated in a standard three-electrode setup in 0.5 M H_2SO_4 solution. The polarization curves of various catalysts, including 2D $h\text{-W}_2\text{N}_3$ flakes, bulk $h\text{-W}_2\text{N}_3$, and 20% Pt/C were shown in the Figure 4a. The 2D $h\text{-W}_2\text{N}_3$ catalyst exhibited much lower onset potential than bulk $h\text{-W}_2\text{N}_3$, which revealed exceptional onset potential of -30.9 mV vs reversible hydrogen electrode (RHE), indicating the outstanding HER activity. Apart from the onset potential, the overpotential corresponding the cathodic current density of 10 mA cm^{-2} is a characteristic

value related to solar fuel conversion, which can be acquired at -98.2 mV for 2D $h\text{-W}_2\text{N}_3$ catalyst. This value is higher than bulk $h\text{-W}_2\text{N}_3$ (-486.9 mV), which demonstrated the 2D morphology of $h\text{-W}_2\text{N}_3$ dramatically influenced HER activity since the 2D morphology can expose sums of active sites to electrolyte.

Evaluation of the hydrogen evolution dynamics is depicted in the Figure 4b, a promising low Tafel slope of $\approx 59 \text{ mV dec}^{-1}$ was acquired from 2D $h\text{-W}_2\text{N}_3$, much superior to the bulk $h\text{-W}_2\text{N}_3$ ($\approx 134 \text{ mV dec}^{-1}$), demonstrating a fast HER kinetics. Its electrical kinetics were also investigated by the electrochemical impedance spectroscopy (EIS) (Figure 4c). 2D $h\text{-W}_2\text{N}_3$ exhibited a small charge transfer resistance of 25Ω at $\eta = 100 \text{ mV}$, much lower than its bulk counterpart. The long-term stability of 2D $h\text{-W}_2\text{N}_3$ was presented in Figure 4d. There is negligible change in the onset potential while the overpotential of 10 mA cm^{-2} cathodic current density degraded has a change only $\approx 7 \text{ mV}$ after 1000 cycles, demonstrating a virtuous stability of this electrocatalyst (Figure 4d). Furthermore, in comparison with other traditional catalysts of VI B transition metal compounds, such as MoS_2 ,^[24] $[\text{Mo}_3\text{S}_{13}]^{2-}$ clusters,^[25] MoP,^[26] Mo_2C ,^[27] WS_2 ,^[28] W_2C ,^[29] and WC,^[30] 2D $h\text{-W}_2\text{N}_3$ presented an extraordinary HER performance (Figure S11).

Infiltrating nitrogen into tungsten lattice with favorable reaction dynamics is the most challenging task up till now. Herein we have synthesized 2D $h\text{-W}_2\text{N}_3$ flakes using salt-templated methods at atmospheric pressure. KCl, as a cheap template, can lower the reaction barrier to facilitate W–N bonding and

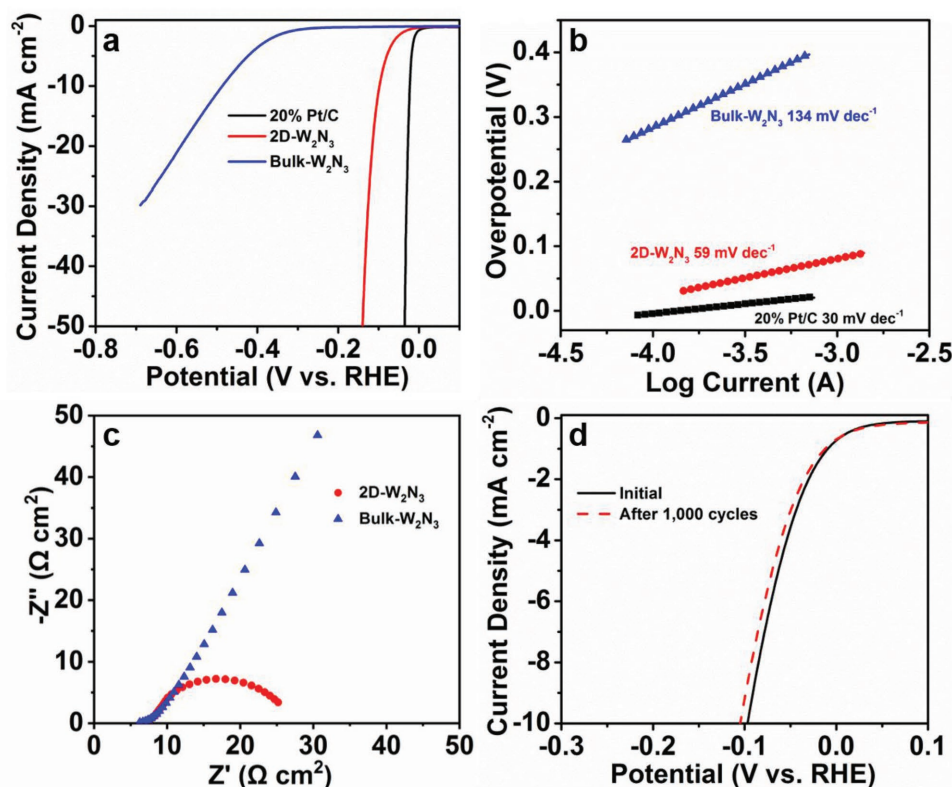


Figure 4. Electrochemical measurements of 2D $h\text{-W}_2\text{N}_3$ for HER in 0.5 M H_2SO_4 . a) Polarization curve of 2D $h\text{-W}_2\text{N}_3$, bulk $h\text{-W}_2\text{N}_3$ and 20 wt% Pt/C. b) Tafel plot of 2D $h\text{-W}_2\text{N}_3$, bulk $h\text{-W}_2\text{N}_3$ and 20 wt% Pt/C. c) Electrochemical impedance spectrum of 2D $h\text{-W}_2\text{N}_3$ at $\eta = 100 \text{ mV}$ in comparison with bulk $h\text{-W}_2\text{N}_3$. d) Polarization curve of 2D $h\text{-W}_2\text{N}_3$ before and after 1000 potential cycles.

two-dimensional growth occurring under confinement effect. The as-synthesized 2D h -W₂N₃ showed a lateral size around 5 μ m with a thickness of \approx 1.5 nm. Compared to the bulk counterpart of 2D h -W₂N₃, N vacancies of the 2D h -W₂N₃ increased when the thickness decreased dramatically, which means that the surface electrical structure might be tuned for specific applications. The 2D h -W₂N₃ exhibits promising HER activity, with the onset potential of -30.9 mV and the overpotential of -98.2 mV at the cathodic current density of 10 mA cm^{-2} in acidic solution. This salt-templated method may provide a new platform for the synthesis of various 2D nitrogen-rich nitrides with distinctive electrical structure, which may be expanded to various applications beyond HER, such as energy storage, solar cells, and mechanics.

Experimental Section

Synthesis of 2D h -W₂N₃: In a typical synthesis, 0.15 g (NH₄)₆H₂W₁₂O₄₀·xH₂O was dispersed in mixed solvent of deionized water (20 mL) and ethanol (10 mL), followed by the addition of 500 g KCl powders into the precursor solution and dry under 60 °C with continuous stirring. The as prepared (NH₄)₆H₂W₁₂O₄₀·xH₂O@KCl was annealed at 750 °C for 5 h at a ramp rate of $1 \text{ }^{\circ}\text{C min}^{-1}$ under a mixture of NH₃ (5%) and Ar, respectively. The product was washed by deionized water to remove KCl and dispersed in deionized water for further studies. The bulk h -W₂N₃ was provided by Prof. S. M. Wang and Prof. D. W. He from Sichuan University.^[10]

Electrochemical Measurements: All electrochemical measurements were performed in 0.5 M H₂SO₄ solution by CHI 660E electrochemical workstation. The counter and reference electrodes were graphite rod and saturated calomel electrode, respectively. A glassy carbon electrode (GCE, 5 mm in diameter) covered by catalyst materials was used as the working electrode. Generally, 2 mg sample suspended in deionized water (400 μ L), then 8 μ L Nafion solution (5.0 wt% Nafion in isopropyl alcohol) was added to the as-obtained solution to form a homogeneous ink after sonication. 10 μ L of the ink was loaded onto GCE by a micropipette and dried in ambient temperature. Before measurements, the samples were repeatedly swept from 0.15 to 0.25 V (vs RHE) in the electrolyte until a steady voltammogram curve was obtained. The polarization curves were scanned from 0 to -0.7 V (vs RHE) at a scan rate of 5 mV s^{-1} . For EIS measurements, range of frequency: $1\text{--}10^4$ Hz, potential: $\eta = 100$ mV. For the stability test, after 1000 cycles of cyclic voltammetry (CV) curves (scan rate: 5 mV s^{-1} , range of potential: $0\text{--}0.1$ V vs RHE).

Characterization: The XRD (X'Pert Pro, PANalytical), Cu K α radiation ($\lambda = 0.1542$ nm) (40 kV and 40 mA), the pattern was collected from 30° to 80°. XPS (ESCALab250), field-emission SEM (FEI Nova 450 Nano), HRTEM (TECNAL and Titan), AFM (Shimadzu), and XAFS were used to explore the structure and morphology of the samples. W L3-edge XAFS spectra were measured at the beamline BL14W1 of the Shanghai Synchrotron Radiation Facility. XAFS data were analyzed with the WinXAS3.1 program.^[31] Theoretical amplitudes and phase-shift functions of W–N and W–W were calculated with the FEFF8.2 code.^[32] using the crystal structural parameters of the W₂N₃ foil. The electron beam energy of the storage ring was 3.5 GeV with a maximum stored current of 300 mA. HAADF image was taken with a JEOL ARM200CF transmission electron microscope equipped with double aberration corrector and a cold field-emission gun operated at 200 kV.

Supporting Information

Supporting Information is available from the Wiley Online Library or from the authors.

Acknowledgements

H.Y., X.Y., and X.X. contributed equally to this work. This work was supported from the National Natural Science Foundation of China (grants 51872101, 61434001, 51322210, 51672097, 51602115, 21727801), the National Program for Support of Top-notch Young Professionals, the program for HUST Academic Frontier Youth Team, the Fundamental Research Funds for the Central Universities (HUST: 2017KFKJC001), National Key Research and Development Program of China (grant 2017YFB0701600, 2014CB932400), Shenzhen Projects for Basic Research (grant JCYJ20170307154206288). We wish to thank Prof. D. W. He and S. M. Wang for providing bulk h -W₂N₃, thank H. Y. Jin for helpful comments on the manuscript, and thank Prof. L. Y. Li for discussing the growth mechanism. We also wish to thank facility support of the Center for Nanoscale Characterization & Devices, WNL0 of Huazhong University of Science and Technology (HUST) and the Analytical and Testing Center of HUST. Tianjin Supercomputing Center is also acknowledged for allowing the use of computational resources including TIANHE-1.

Conflict of Interest

The authors declare no conflict of interest.

Keywords

2D materials, atmospheric-pressure synthesis, electrocatalysis, nitrogen-rich, transition metal nitrides

Received: August 31, 2018

Revised: September 28, 2018

Published online: October 24, 2018

- [1] P. Urbankowski, B. Anasori, K. Hantanasirisakul, L. Yang, L. Zhang, B. Haines, S. J. May, S. J. L. Billinge, Y. Gogotsi, *Nanoscale* **2017**, 9, 17722.
- [2] P. Simon, Y. Gogotsi, *Nat. Mater.* **2008**, 7, 845.
- [3] X. Xiao, X. Peng, H. Jin, T. Li, C. Zhang, B. Gao, B. Hu, K. Huo, J. Zhou, *Adv. Mater.* **2013**, 25, 5091.
- [4] S. Wang, H. Ge, S. Sun, J. Zhang, F. Liu, X. Wen, X. Yu, L. Wang, Y. Zhang, H. Xu, J. C. Neuefeind, Z. Qin, C. Chen, C. Jin, Y. Li, D. He, Y. Zhao, *J. Am. Chem. Soc.* **2015**, 137, 4815.
- [5] S. Yamanaka, K.-i. Hotehama, H. Kawaji, *Nature* **1998**, 392, 580.
- [6] H.-M. Kim, Y.-H. Cho, H. Lee, S. I. Kim, S. R. Ryu, D. Y. Kim, T. W. Kang, K. S. Chung, *Nano Lett.* **2004**, 4, 1059.
- [7] T. Kuykendall, P. J. Pauzauskie, Y. Zhang, J. Goldberger, D. Sirbulu, J. Denlinger, P. Yang, *Nat. Mater.* **2004**, 3, 524.
- [8] A. Salamat, A. L. Hector, P. Kroll, P. F. McMillan, *Coord. Chem. Rev.* **2013**, 257, 2063.
- [9] H. A. Wriedt, *Bull. Alloy Phase Diagrams* **1989**, 10, 358.
- [10] S. Wang, X. Yu, Z. Lin, R. Zhang, D. He, J. Qin, J. Zhu, J. Han, L. Wang, H.-k. Mao, J. Zhang, Y. Zhao, *Chem. Mater.* **2012**, 24, 3023.
- [11] Y. Zheng, Y. Jiao, Y. Zhu, L. H. Li, Y. Han, Y. Chen, A. Du, M. Jaroniec, S. Z. Qiao, *Nat. Commun.* **2014**, 5, 3783.
- [12] D. Voiry, H. Yamaguchi, J. Li, R. Silva, D. C. B. Alves, T. Fujita, M. Chen, T. Asefa, V. B. Shenoy, G. Eda, M. Chhowalla, *Nat. Mater.* **2013**, 12, 850.
- [13] D. Deng, K. S. Novoselov, Q. Fu, N. Zheng, Z. Tian, X. Bao, *Nat. Nanotechnol.* **2016**, 11, 218.
- [14] C. Tan, X. Cao, X. J. Wu, Q. He, J. Yang, X. Zhang, J. Chen, W. Zhao, S. Han, G. H. Nam, M. Sindoro, H. Zhang, *Chem. Rev.* **2017**, 117, 6225.

- [15] D. Choi, P. N. Kumta, *J. Am. Ceram. Soc.* **2007**, *90*, 3113.
- [16] W.-F. Chen, J. T. Muckerman, E. Fujita, *Chem. Commun.* **2013**, *49*, 8896.
- [17] X. Xiao, H. Song, S. Lin, Y. Zhou, X. Zhan, Z. Hu, Q. Zhang, J. Sun, B. Yang, T. Li, L. Jiao, J. Zhou, J. Tang, Y. Gogotsi, *Nat. Commun.* **2016**, *7*, 11296.
- [18] J. Yang, D. Voiry, S. J. Ahn, D. Kang, A. Y. Kim, M. Chhowalla, H. S. Shin, *Angew. Chem., Int. Ed.* **2013**, *52*, 13751.
- [19] R. Chen, T. Zhao, W. Wu, F. Wu, L. Li, J. Qian, R. Xu, H. Wu, H. M. Albishri, A. S. Al-Bogami, D. A. El-Hady, J. Lu, K. Amine, *Nano Lett.* **2014**, *14*, 5899.
- [20] J. A. P. Taborda, H. R. Landázuri, L. P. V. Londoño, *IEEE Sens. J.* **2016**, *16*, 359.
- [21] S. Gao, Z. Sun, W. Liu, X. Jiao, X. Zu, Q. Hu, Y. Sun, T. Yao, W. Zhang, S. Wei, Y. Xie, *Nat. Commun.* **2017**, *8*, 14503.
- [22] K. Xu, P. Chen, X. Li, Y. Tong, H. Ding, X. Wu, W. Chu, Z. Peng, C. Wu, Y. Xie, *J. Am. Chem. Soc.* **2015**, *137*, 4119.
- [23] Z. Zeng, K.-C. Chang, J. Kubal, N. M. Markovic, J. Greeley, *Nat. Energy* **2017**, *2*, 17070.
- [24] J. Hu, B. Huang, C. Zhang, Z. Wang, Y. An, D. Zhou, H. Lin, M. K. H. Leung, S. Yang, *Energy Environ. Sci.* **2017**, *10*, 593.
- [25] J. Kibsgaard, T. F. Jaramillo, F. Besenbacher, *Nat. Chem.* **2014**, *6*, 248.
- [26] Z. Xing, Q. Liu, A. M. Asiri, X. Sun, *Adv. Mater.* **2014**, *26*, 5702.
- [27] F.-X. Ma, H. B. Wu, B. Y. Xia, C.-Y. Xu, X. W. Lou, *Angew. Chem., Int. Ed.* **2015**, *54*, 15395.
- [28] M. A. Lukowski, A. S. Daniel, C. R. English, F. Meng, A. Forticaux, R. J. Hamers, S. Jin, *Energy Environ. Sci.* **2014**, *7*, 2608.
- [29] Q. Gong, Y. Wang, Q. Hu, J. Zhou, R. Feng, P. N. Duchesne, P. Zhang, F. Chen, N. Han, Y. Li, C. Jin, Y. Li, S.-T. Lee, *Nat. Commun.* **2016**, *7*, 13216.
- [30] M. Zeng, Y. Chen, J. Li, H. Xue, R. G. Mendes, J. Liu, T. Zhang, M. H. Rümmeli, L. Fu, *Nano Energy* **2017**, *33*, 356.
- [31] T. Ressler, *J. Synchrotron Radiat.* **1998**, *5*, 118.
- [32] A. L. Ankudinov, B. Ravel, J. J. Rehr, S. D. Conradson, *Phys. Rev. B* **1998**, *58*, 7565.